



Evaluating the Impact of Fly Ash Content on the Dry Sliding Wear Behaviour of Al–Si–Mg–Cu Metal Matrix Composite for Lightweight Application

Karthik V. Shankar^{1,2} · Vaira Vignesh Ramalingam³ · G. P. Gokul Krishna¹ · Devaprasad Padmakumar¹ · Midun Raj Leena¹ · Amal Amal¹ · Gokul Reghunath¹ · Jithin Vishnu^{1,2} · Rakesh Krishnan¹

Received: 31 May 2023 / Revised: 31 October 2023 / Accepted: 7 November 2023 / Published online: 12 December 2023
© The Author(s), under exclusive licence to Springer Nature Switzerland AG 2023

Abstract

In this work, the A354 alloy is reinforced with fly ash ceramic particles to study the dry sliding wear features of the developed aluminium metal matrix composite (AMMC). The metal matrix composite (MMC) of varying wt.% (5, 10, and 15) of fly ash was synthesized through a liquid metallurgy route. The developed AMMC was characterized by microstructure, hardness, density, wear rate, and coefficient of friction. Observations indicate that reinforcing 5 weight % of fly ash particles enhances the developed MMC's hardness, wear resistance, and density. Specifically, samples with 5 wt.% of fly ash have shown the highest microhardness values. The dry sliding wear analysis was performed at room temperature using a tribometer per ASTM G99 standard. Results show that the specimen reinforced with 5 wt.% of fly ash has the least specific wear rate compared to all other specimens. The least wear rate obtained is at a normal load of 15N and a sliding velocity of 3 m/s. The wear test also divulges that the coefficient of friction was highest in samples tested at a sliding velocity of 3 m/s and 15 N load. Further, the wear properties of the specimens were characterized using SEM and EDS analyses. Hence, the investigation proved that adding fly ash in a minimal weight percentage (5 wt.%) enhances the potential of A354 MMC to be used in developing cylinder heads and other such drive train components.

Keywords Hardness · Wear rate · Engine cylinder · Coefficient of friction · A354 · Al–Si–Mg–Cu/fly ash

1 Introduction

Aluminium and its alloys find extensive applications in almost all sectors, especially the automotive and aerospace industries. The main reason behind this is its low density and excellent specific strength. These alloys are a perfect replacement for cast iron in casting most drive train components of commercial vehicles as it caters to reducing the mass of engine blocks and such components, thereby

cutting down the vehicle's kerb weight [1]. Manufacturing automotive components, especially cylinder heads, demand good castability, reduced weight, and excellent mechanical properties; hence, aluminium alloys are a good candidate. Another beneficial aspect of using these alloys is the environmental impact. The environmental impact surveys have revealed that almost 20% or more of harmful CO₂ emissions come from vehicles [2, 3]. Using non-renewable resources at a broader rate has posed a severe environmental threat. So, as manufacturers started to experience the pressure to minimize emissions and consumption, a need arose to produce more efficient vehicles [3–8]. Hence, aluminium and its alloys can be a panacea regarding its economic viability and properties.

However, far-fledged applications of aluminium alloys are hampered by undesirable lower hardness, susceptibility to wear, reduced scratch resistance, etc. For instance, the mechanical and thermal loads on a cylinder head made of casting will be very high [2]. Aluminium and its alloys will not be able to withstand such heavy load abrasions

✉ Karthik V. Shankar
karthikvs@am.amrita.edu

¹ Department of Mechanical Engineering, Amrita Vishwa Vidyapeetham, Amritapuri 690525, India

² Centre for Flexible Electronics and Advanced Materials, Amrita Vishwa Vidyapeetham, Amritapuri 690525, India

³ Department of Mechanical Engineering, Amrita School of Engineering, Amrita Vishwa Vidyapeetham, Coimbatore 641112, India

or thermal shocks, thereby getting restricted from usage despite having other unique properties. Many advancements were brought to increase the durability and hardness of the Al metal/alloys and their processing. These include modern casting methods, solution treatment, and natural and artificial aging. Research shows that the mechanical properties of aluminium alloys can be augmented by about 25–30% by solutionising and aging techniques characterized by non-standard parameters [3]. The addition of ceramic reinforcements and fabrication of composites open broad pathways to impart the desired properties of Al. Such fabrication of MMCs from the Al alloy matrix has displayed outstanding properties, enhancing the overall usability.

MMCs possess high mechanical properties, specific modulus, reduced wear rate, less density, and improved hardness [9, 10]. These properties depend heavily on the reinforcement added to the metal matrix. A wide array of reinforcement materials is found nowadays, and their addition adds to the extra cost of the product. In effect, most MMCs are expensive. Since Al alloys have extensive usage and demand, it is essential to check the cost of the reinforcement that is being added. So, many researchers follow this trend to identify the comparatively less expensive reinforcement that generates MMC with high properties [11]. In this aspect, fly ash is regarded as a particle with less cost and capable of enhancing properties to a greater extent. Fly ash is an affordable by-product of burning coal, produced primarily in thermal power plants and cement factories. [12]. The peculiarity is that this solid-waste product is produced in enormous quantities, so its diverted usage is, in fact, a financially and environmentally viable situation. Fly ash is extracted from exhaust gases by mechanical or electrostatic precipitators. It comprises oxides with varying mineral content according to the coal used [12, 13]. Some of the significant constituents of fly ash include silicon, iron, calcium, etc., which impart a ceramic nature to the substance [14–16].

The properties of alloys made from aluminium are often greatly influenced by the composition and the manufacturing route (for the fabrication of MMCs, like powder metallurgy, hot pressing, and other molten metal methods). However, during the fabrication processes, it has been observed that ceramic reinforcements react with molten metal and form solid reaction products in the matrix, eventually deteriorating the desirable properties. Stir casting represents an effective fabrication method for fabricating MMC, especially with an aluminium alloy matrix [17–20]. Stir casting is comparatively less expensive and enables a high production rate. Aybar et al. [21] investigated the SiC, Al₂O₃, and graphene reinforcements and analyzed their distribution in the base alloy matrix. A solid conclusion arrived from that research work [13] was that the stir casting setup or liquid metallurgy route is the most feasible and efficient route to

impart reinforcement particles which are in solid form, into a molten aluminium alloy matrix.

Research has shown that the A356 and A354 alloy series of aluminium, with their remarkable castability and intermediate mechanical properties, is ideal for molded automotive parts such as cylinder heads [22, 23]. The impact of fly ash content on the mechanical, microstructural, and physical properties of Fe–Cu–C alloy sintered using a powder metallurgy process was recently examined by Motta et al. [24]. The alloy's mechanical and wear resistance was enhanced, and its density was decreased by adding fly ash content. The impact of bio-silicon ceramic particles on the mechanical and thermal characteristics of Al-10 Mg bonded with waste fly ash for automotive applications was investigated by Venkatesh et al. [25]. Good thermal properties were demonstrated by reinforcing Al alloy with 5 weight percent fly ash and 1 weight percent bio-ceramic Si₃N₄-reinforced (p). Pal et al. [26] investigated the mechanical properties of an Al5456 alloy reinforced with a SiC/fly ash content. The created hybrid composites' mechanical properties were improved by adding ceramic particles. Son et al.'s research [27] revealed that T5 aging enhanced the Al–Si–Mg–Cu alloy's mechanical characteristics. The authors also examined the impact of the melt-holding temperature on the mechanical characteristics and microstructure of the alloy that was created. Zang et al. [28] looked into the effects of Cu concentration and Mg/Si ratio on the tensile strength of A354 alloy. The Mg/Si ratio was found to increase grain size while decreasing particle size by the authors. Despite A354 being identified as a promising material for developing cylinder heads and other drive train components, experiments and research on A354 alloy are significantly less. In addition, a thorough study of this alloy with the proper reinforcement choice could reveal its excellent mechanical behaviour to yield a promising use in developing cylinder heads and such engine components. Since fly ash is identified as an inexpensive waste product produced in large quantities and harms the environment, attention to its recycling/reuse is a prime factor. Thus, the current research investigates the addition of fly ash onto the A354 base alloy to improve the properties and thoroughly studies the morphological and tribological behaviour of the fabricated MMCs.

2 Materials and Methods

2.1 Materials

Automobile parts are frequently made of the A354 alloy, specially molded pieces like cylinder heads. To create an ingot of A354 (Al–Si–Mg–Cu), 99.9% pure Al, Si, Mg, and Cu were obtained and melted in an electric furnace inside a clay graphite crucible. After performing an arc spectrometric

Table 1 Composition of as-received alloy (A354)

Elements	Al	Si	Mg	Cu
Wt.%	Bal	6.9	0.39	2.8

Table 2 Samples studied in this research

Sample Code	Matrix	Wt.% ceramic Reinforcement Fly ash
A	A354—Al—Si—Mg—Cu	0
AF ₅	A354—Al—Si—Mg—Cu	5
AF ₁₀	A354—Al—Si—Mg—Cu	10
AF ₁₅	A354—Al—Si—Mg—Cu	15

investigation on the cast ingot, the alloy was found to vary by around 0.3 weight percent from its nominal composition. Table 1 lists the precise weight percentages of Al, Si, Mg, and Cu that make up this alloy.

2.2 Fabrication of MMC

The obtained specimen was cast between 760 and 780 °C in temperature. The melting process was carried out in an electric furnace that was equipped with a graphite stirrer to ensure that the fly ash particles in the base alloy were mixed uniformly. The reinforcement was preheated in the furnace to a temperature of 300 °C before being added gradually to the melt using a hopper. As indicated in Table 2, the current study used different weight percentages (5, 10, and 15) of fly ash as reinforcement. The fly ash ceramic particle images used in this study were obtained using energy dispersive spectroscopy (Make: Oxford Instruments; Model: Ultim Max) and field emission scanning electron microscopy (Fig. 1).

The ceramic particle's average size was 5 µm, according to the analysis done with ImageJ software (software version: 1.53t). To limit any possible oxidation reactions of the melt, the entire melting process was carried out in an atmosphere of inert gas (Ar). Stirring was done for nearly ten minutes at 200 rpm in order to successfully mix the reinforcement within the alloy matrix. To make the fly ash more wettable with the Al alloy, a small trace (1 weight percent) of magnesium was added to the melting furnace. Melted metal was poured into a permanently heated Lubrikote-coated mould after it had been mixed to create cast specimens with dimensions of ~32 mm by 156 mm in length. The composition of the as-cast alloy was analysed by Arc spectroscopy (Foundry master, Germany) study to ascertain the presence of alloying elements in the A354 alloy. The average value of about 5 tested specimens was calculated, and the elemental

distribution of A354 alloy is shown in Table 1. Moreover, the morphological analysis confirms zero evidence of cast defects like porosity. The fabricated samples were machined and brought to suitable dimensions for microstructure, hardness, and wear testing. The prepared MMC specimens were then characterized using FESEM-EDS and an X-ray diffractometer (Make: Rigaku; Model: Ultima 4). Figure 2 depicts the experimental methodology followed in this present investigation.

2.3 Density

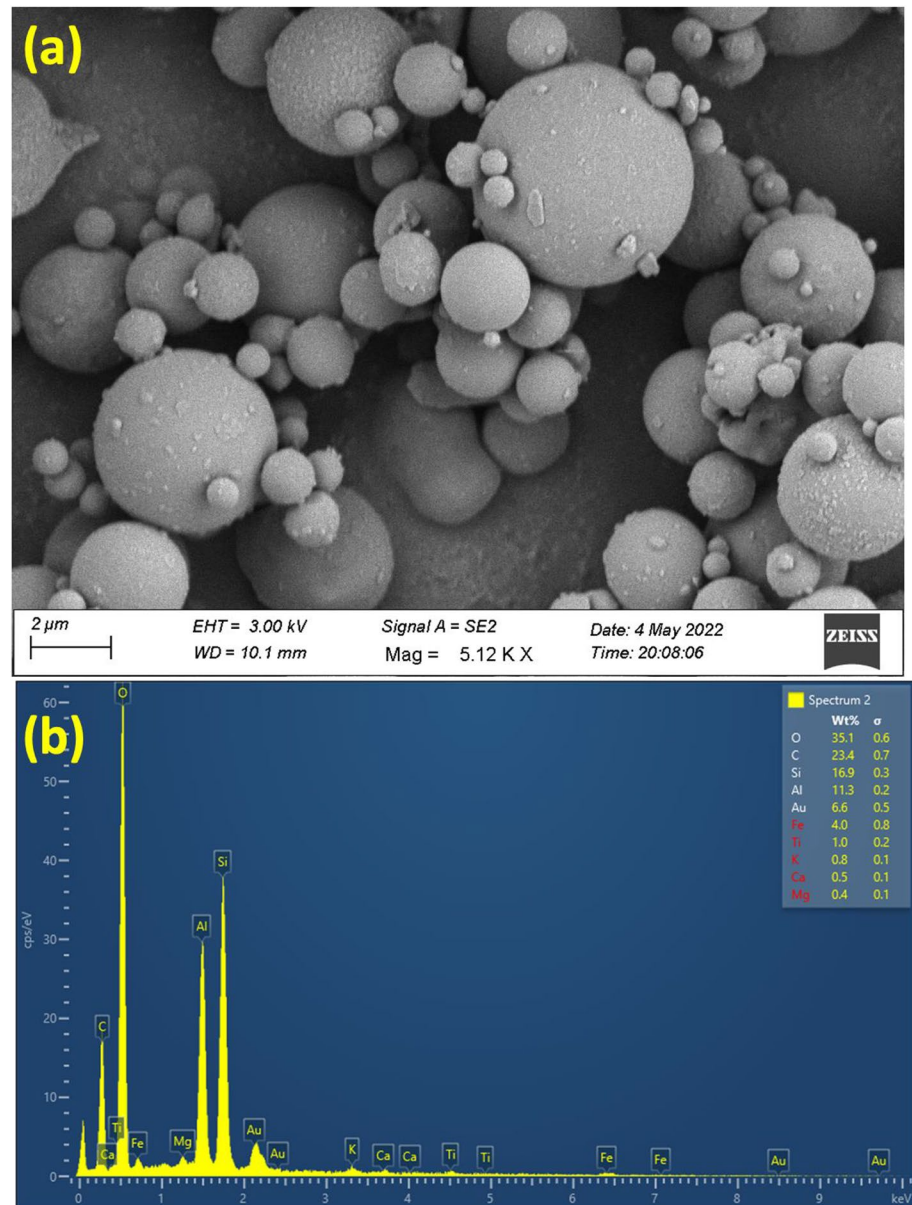
Figure 3 depicts the cast specimen's experimental and theoretical density values. Archimedes' principle was utilized to ascertain the experimental density values for all the developed MMCs. The experimental density analysis was based on the ASTM B96213 standard. Samples' theoretical values were obtained through the rule of mixtures. Theoretical density is higher than experimentally measured values, as shown in Fig. 3. Equation (1) was utilized to evaluate the theoretical density of the manufactured composites. The density of the aluminium MMC is denoted by $\rho_{(MMC)}$. At the same time, the volume fractions of the matrix and reinforced ceramic particles are represented by $V_{f(m)}$ and $V_{f(p)}$, respectively. Weight percentages of alloy compositions were converted to volume fractions for easy calculation before the computation of theoretical densities.

$$\rho_{(MMC)} = \rho_m \times V_{f(m)} + \rho_p \times V_{f(p)} \quad (1)$$

2.4 Microstructure and Hardness Test

The as-cast A354 alloy and the fabricated MMC discussed in this study were examined for microstructure and other constituent details using a Field Emission Scanning Electron Microscope (FESEM) equipped with an Energy Dispersive Spectroscopy (EDS). The samples were cut to 10 × 10 mm for the FESEM analysis. An automatic disc grinder with various discs with grit sizes from 400 to 2000 was used to polish these specimens. These samples were polished using a slurry of diamond particles to get a better surface finish. The typical etchant was Keller's reagent. Vickers Microhardness Tester (Mitutoyo, Kawasaki, Japan; Model: HM-210 A) was used to measure the hardness values of MMC manufactured per ASTM E-384 standard and base alloy (A354). Before the hardness analysis, the samples' surfaces were polished with silicon carbide paper (also known as emery paper), which is readily available in the market. For about 30 s, a 100 gmf load was applied to the sample surface. As shown in Table 2, indentations were made at five different

Fig. 1 **a** FESEM image showing the morphology of fly ash particles and **b** corresponding EDX analysis of fly ash particles



locations on the specimen surface, and the material's average hardness value was evaluated.

2.5 Tribology Test

Using a CNC turning center (DENFORD, UK, Model: Turn-270 Pro), the specimens for the tribological tests were machined from the castings into pins with a diameter of 10 mm and a length of 50 mm. The specimens were then polished following ASTM E3-11 standard. A pin-on-disc tribometer conducted tribology tests in ambient conditions (temperature 29 °C, humidity 73%). according to the specifications given in ASTM G99-17 (Ducom; Model: TR-20NEO). During testing, the pins were brought into contact with the counter disc. EN31 steel, with a hardness of 62

HRC, was used to make the counter disc. The parameters used for the tribological testing were the axial load of 5, 10, and 15 N, the sliding velocity of 1, 2, and 3 m/s, and the sliding distance of 1000 m. The average wear rate and friction coefficient were reported after the tribological tests were run in triplicate. Table 3 lists the experimental design used for the tribological tests.

3 Results and Discussion

3.1 Microstructural and Phase Analysis

Figure 4a displays the microstructural images of the as-cast A354 alloy. It consists of a eutectic Si phase that is rich in

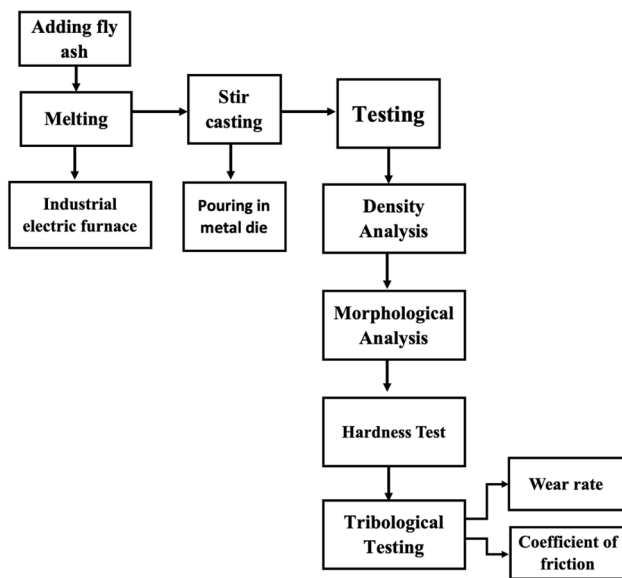


Fig. 2 Experimental methodology

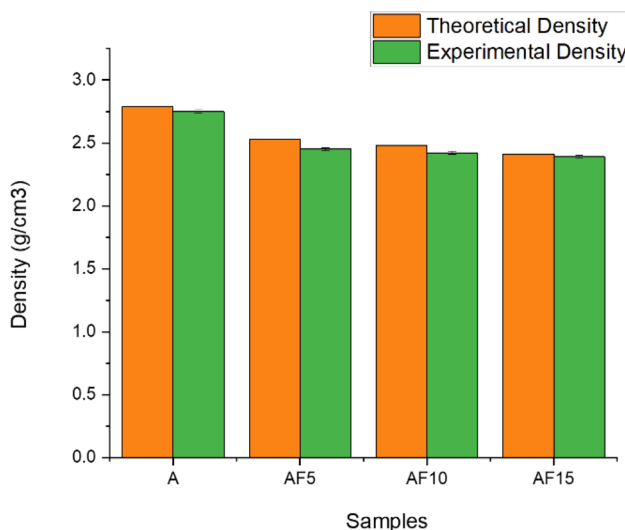


Fig. 3 Density values for developed alloy and composites

Table 3 Experimental design for tribological test

Sl. No	Specimen Code	Axial load (N)	Sliding velocity (m/s)
1	A, AF ₅ , AF ₁₀ , AF ₁₅	5, 10, 15	3
2	A, AF ₅ , AF ₁₀ , AF ₁₅	15	1, 2, 3

-Al. Certain intermetallic phases were also discovered in the as-cast alloy's grain boundary areas. Samples of the AF₅, AF₁₀, and AF₁₅ microstructures are indicated in Fig. 4b–d,

respectively. The structure of the eutectic Si phase was altered by adding reinforcement to the A354 alloy, as seen in Fig. 4b–d. Our prior study investigated these produced composites in-depth using EDS analysis and elemental mapping [1]. The FESEM micrograph of the A354 alloy with reinforcement additions of 5 and 10 weight percentages is shown in Fig. 4b and c.

The Image shows that the A354 alloy with a 5 weight percent addition of fly ash had the best mixing of ceramic particles. Additionally, AF₅ and AF₁₀ have the same distribution of reinforcement particles. All of these point to an efficient MMC fabrication process. However, SEM images of the A354 alloy with a 15 wt% addition of fly ash are depicted in Fig. 4d. The reinforced particles are believed to be agglomerated within the A354 matrix, according to Fig. 4d. An uneven reinforcement mixture can, therefore, compromise this produced MMC's mechanical behaviour [29, 30].

An XRD examination of the aluminium alloy and its composites was carried out to validate the presence of fly ash and intermediate phases. The A354 alloy sample has α -Al and eutectic Si, while the fly ash-reinforced alloy has α -Al (JCPDS card #89-4184), eutectic Si (JCPDS card #27-1402), and quartz/mullite (JCPDS card #46-1045) peaks, as shown in Fig. 5. The presence of additional peaks can be attributed to the base alloy's increased fly ash percentage. The acquired results show that the alloy and its composites were manufactured successfully.

3.2 Microhardness

Figure 6 depicts the Vickers hardness of all the developed samples with the error bar. Analyzing the average hardness values of samples A, AF₅, AF₁₀, and AF₁₅ after the Vickers hardness test, sample AF₅ has shown a comparatively higher hardness value. The reason for this increased hardness of AF₅ can be the amazing bonding of fly ash within the base alloy matrix. Despite having lesser fly ash content than in the other two samples (AF₁₀ and AF₁₅), AF₅ showed a superior hardness, suggesting that a lower fly ash content helps greatly in grain refinement than the ones with higher fly ash content. This highlights the perfect mixing of reinforcement particles in the base alloy matrix. Furthermore, dislocation hardening can also be considered a reason for the increased hardness of this MMC [1].

The applied load was directly transferred to the reinforcement particles. Rather than just sustaining the load, these reinforcement particles have restricted plastic deformation geometrically. This created enough dislocations within the matrix to handle the applied load, thereby increasing the dislocation density, which resulted in dislocation hardening. Dispersion hardening and Orowan strengthening can also be attributed as reasons for the increased hardness of this MMC from its baseline alloy. Even though increased resistance

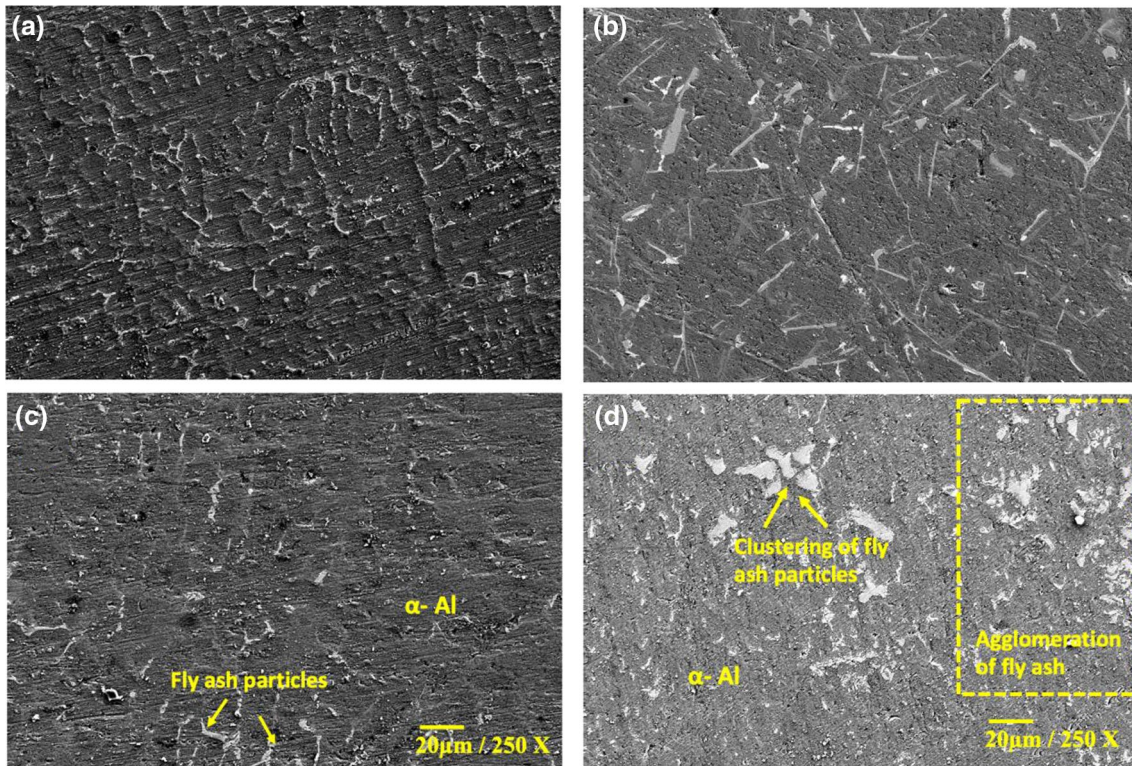
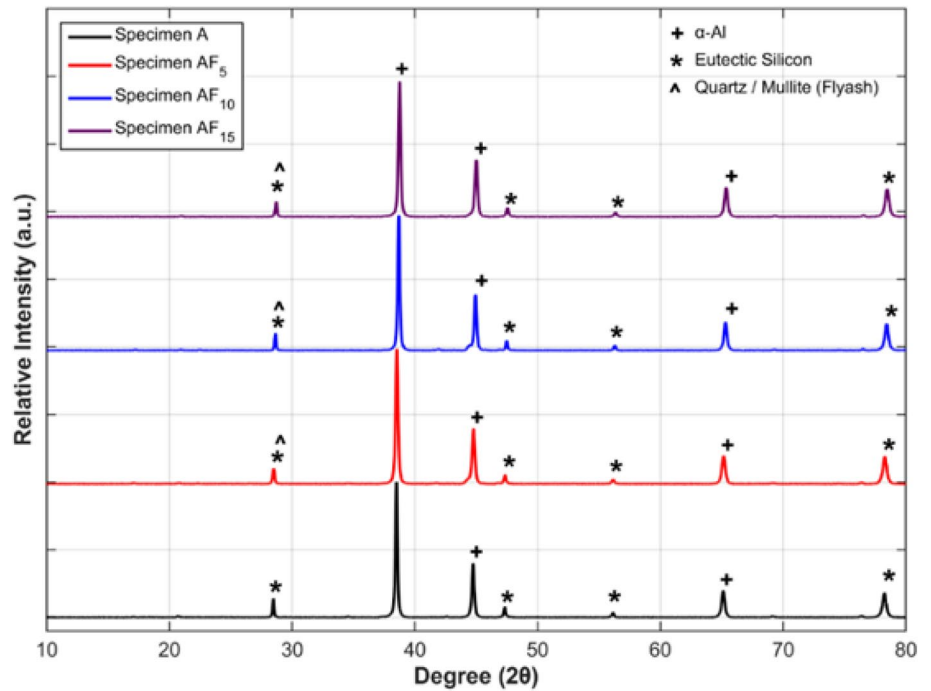


Fig. 4 FESEM images of the sample **a** A **b** AF₅ **c** AF₁₀ **d** AF₁₅

Fig. 5 XRD analysis of developed alloy and composites. Reprinted with permission from MDPI [1]



to plastic deformation was expected as the percentage of reinforcement increased, the hardness value obtained for samples with 10 wt.% (AF₁₀) and 15 wt.% (AF₁₅) were

comparatively lower. This is due to the agglomeration of reinforced particles in the A354 matrix caused by irregular mixing [1].

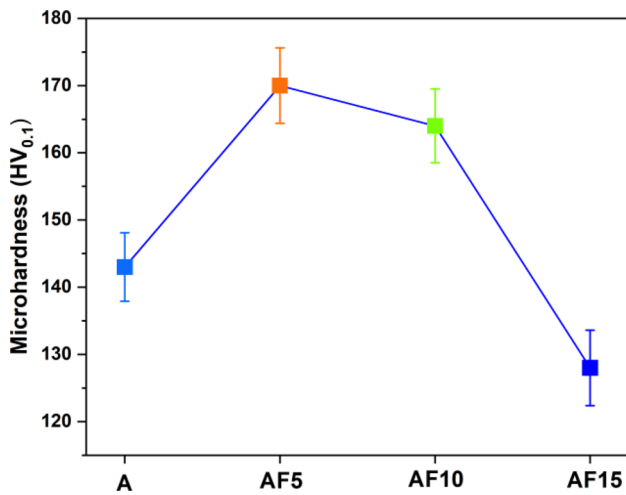


Fig. 6 Hardness values of various cast samples

3.3 Tribological Investigation

3.3.1 Influence of Load on the SWR and Friction Coefficient

Table 4 represents the average SWR (specific wear rate) and coefficient of friction (COF) of developed alloy and MMCs on varying loads and for a sliding distance of 1000 m. It can be inferred from Table 4 that, as the load is subjected to variation, significant changes also occur in the coefficient of friction and particular wear rate values.

The specific wear rate of fabricated composite specimens worn at varying weights (5, 10, and 15 N) and sliding at a speed of 3 m/s is displayed in Fig. 7a. At a load of 5 N, the base material among the evaluated specimens showed a maximum wear rate of 0.00005 mm³/Nm. The specimens' wear rate and reinforcing fraction showed a linear trend at a load of 5 N. Specimen AF5 showed the

Table 4 Average SWR of MMC on changing load

Sample No	Sample code	Applied load (N)	Sliding velocity (m/s)	Average specific wear rate values $\times 10^{-5}$ (mm ³ /Nm)	Coefficient of friction values (COF)
1	A	5	3	5.00 \pm 0.065	0.315 \pm 0.01
2	A	10	3	6.52 \pm 0.072	0.324 \pm 0.01
3	A	15	3	4.31 \pm 0.063	0.332 \pm 0.03
7	AF ₅	5	3	3.61 \pm 0.045	0.416 \pm 0.03
8	AF ₅	10	3	4.31 \pm 0.022	0.445 \pm 0.23
9	AF ₅	15	3	3.59 \pm 0.011	0.458 \pm 0.01
13	AF ₁₀	5	3	4.54 \pm 0.023	0.543 \pm 0.04
14	AF ₁₀	10	3	4.81 \pm 0.071	0.551 \pm 0.03
15	AF ₁₀	15	3	3.93 \pm 0.044	0.564 \pm 0.01
19	AF ₁₅	5	3	4.83 \pm 0.01	0.556 \pm 0.02
20	AF ₁₅	10	3	4.91 \pm 0.062	0.561 \pm 0.01
21	AF ₁₅	15	3	3.63 \pm 0.032	0.569 \pm 0.01

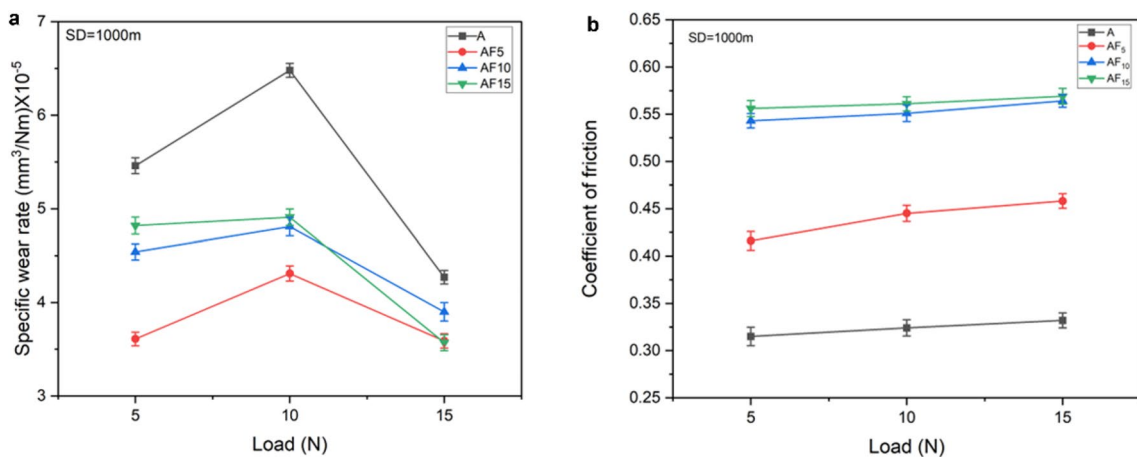


Fig. 7 Influence of load on the base material and developed composite specimens a Specific wear rate; b Coefficient of friction

lowest wear rate, measuring $0.0000361 \text{ mm}^3/\text{Nm}$, 27.8% less than the base material. An analogous pattern was observed at a load of 10 N. At $0.0000431 \text{ mm}^3/\text{Nm}$, the specimen AF₅ displayed the lowest wear rate, while the base material displayed the highest at $0.0000652 \text{ mm}^3/\text{Nm}$. At an axial stress of 10 N, there observed a minor variation in the wear rate (10.39%) between the specimens AF₅ and AF₁₀. The typical load of 15 N showed a noticeable decrease in the specimens' wear rate. $0.0000431 \text{ mm}^3/\text{Nm}$ was the basis material wear rate at 15 N, 13.8% smaller than the base material wear rate at 5 N. Similarly, the wear rates of the specimens AF₅, AF₁₀, and AF₁₅ worn at 15 N were lower than those worn at 5 N.

The COF of the base material and developed composite specimens worn at a sliding velocity of 3 m/s and varied loads (5, 10 and 15 N) is shown in Fig. 7b. The coefficient of friction was the least for the base material (0.30 and 0.35) at all the test loads. The coefficient of friction was between 0.40 and 0.45 for specimen AF₅, lower than the specimen AF₁₀ and AF₁₅. The specimens AF₁₀ and AF₁₅ had no significant variation in the coefficient of friction at all the test loads. The COF varied between 0.53 and 0.58 for the specimen AF₁₀ and AF₁₅. The general trend was that the coefficient of friction increased when the load was raised from 5 to 15 N for all the specimens (base material and developed composite specimens). The mechanism of wear and factors attributed to such phenomenon are described in the proceeding section.

3.3.2 Wear Mechanism Associated with Load Variation

The worn surface morphology of the base material at the normal loads of 5 N and 15 N is shown in Fig. 11a, b, respectively. Figure 11a shows the delamination zone and scoring on the worn surface of the base material at the normal load of 5 N. The separation of the material layer along the plane parallel to the surface indicates high-order adhesive wear of the specimen. The elemental composition of the specimen shown in Fig. 8a indicates that the relative composition of the O was lesser than Al. Hence, the surface of the specimen was not oxidized in the course of the wear test. The wear debris and cracks were observed on the worn surface of the base material at the normal load of 15 N, as shown in Fig. 11b. The physical characteristics indicate high-order adhesive wear of the base material. The phase composition analysis depicted in Fig. 9 revealed less intense peaks for Al₂O₃. Also, oxides of Fe were not observed in phase composition analysis on base material at the normal load of 15 N. The widening of peaks indicated an intense deformation of the specimen.

Chips and pits were observed on the worn surface of the specimen AF₅ at the normal load of 5 N, as represented in Fig. 10c. A relatively lesser fraction of wear debris was observed in specimen AF₅ than in the base material. Hence, the specimen AF₅ had worn in a mild adhesive wear regime. The elemental composition, depicted in Fig. 8b, shows that O had a lower relative composition than Al and Fe. Hence, during the wear test, the surface did not oxidize. The higher

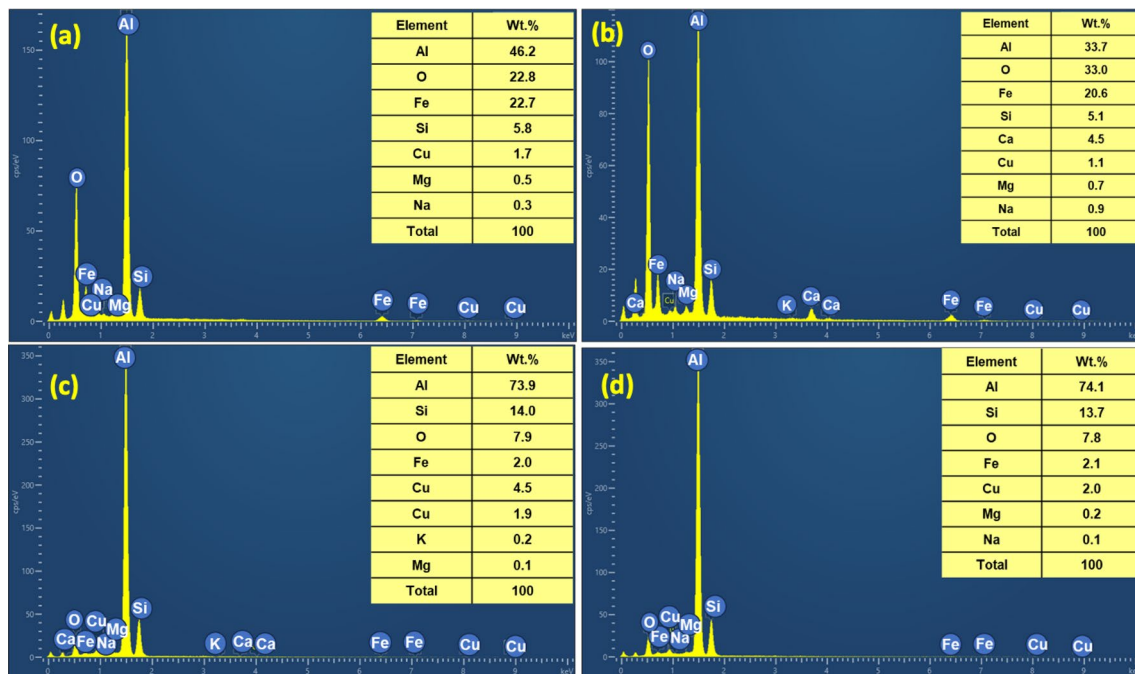
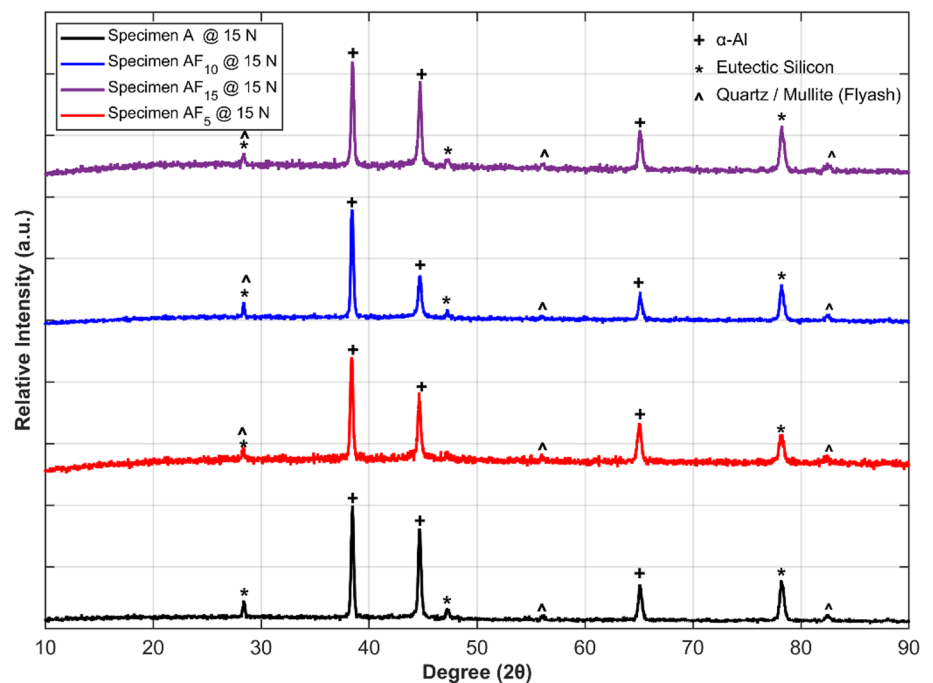


Fig. 8 Elemental composition at an axial load of 5 N **a** Specimen A; **b** Specimen AF₅; **c** Specimen AF₁₀; **d** Specimen AF₁₅

Fig. 9 Phase composition analysis of developed alloy and composites for low wear rate at 15N



fraction of Fe indicated wear debris formation from the counter disc and partial diffusion of Fe towards the specimen. A roughly circular cavity and localized aberrations were observed on the surface at the normal load of 15 N in Fig. 10d. The features indicate mild adhesive wear of the specimen AF₅.

Similarly, the wear rate of the specimen AF₅ was 27.8% and 16.70% less than the base material at the normal load of 5 N and 15 N, respectively. Like the base material, the phase composition analysis depicted in Fig. 9 showed peak indexing for Al₂O₃. Moreover, the phase composition did not reveal any Fe oxides. Also, the broadening of peaks suggested that the material had undergone significant deformation.

The worn surface morphology of the specimen AF₁₀ at the normal load of 5 N had shallow groove and delamination, as represented in Fig. 10e. The grooves and delamination indicate a transformative wear mechanism from mild to severe adhesive wear. Consequently, the wear rate was 25.78% higher than the specimen AF₅ at the normal load of 5 N. Figure 8c establishes that the elemental composition of O was lesser than Al and Fe. That, in turn, evidenced the non-oxidation of the surface during the wear test. The lesser Fe fraction suggested the partial diffusion of Fe into the specimen. The specimen AF₁₀ had a sharp transition from mild adhesive wear to severe adhesive wear, as evidenced through surface galling shown in Fig. 10f at a load of 15 N. The fraction of wear debris increased with the fraction of reinforcements. The wear debris intensified the material removal during the tribology test, resulting in

severe adhesive wear of the specimen. Likely, the wear rate of specimen AF₁₀ was 25.76% higher than specimen AF₅. Al₂O₃ had fewer pronounced peaks in the phase composition analysis (Fig. 9). Moreover, phase composition analysis failed to find any Fe oxides. Further, the widening of peaks evidenced that the specimen AF₁₀ had experienced severe deformation at a load of 15 N.

Deep grooves were observed on the worn surface of the specimen AF₁₅ at the normal load of 5 N in Fig. 10g. The removal of reinforcement particles in the form of wear debris ascribed to the formation of grooves, as the specimen AF₁₅ slid over the wear debris against the counter disc. The characteristic features indicate the abrasive wear phenomenon. The concentration of O was lesser than Al and Fe, according to Fig. 9d. The ratio between the concentration of Al/Fe and O did not adequately specify the formation of oxides. The lower Fe fraction on the worn surface suggested a partial diffusion of Fe. Usually, the abrasive wear mechanism would be mapped to the high wear rate of the specimen. However, the wear rate of the specimen AF₁₅ was lesser than the base material at the normal load of 5 N (high-order adhesive wear). The reinforcement particles in specimen AF₁₅ restricted the localised deformation, increasing the wear resistance. In the phase composition study, Al₂O₃ peaks were less distinct (Fig. 9). The phase composition analysis revealed no Fe oxides. Moreover, specimen AF₁₅ suffered significant deformation at a load of 15 N, as shown by the widening of the peaks.

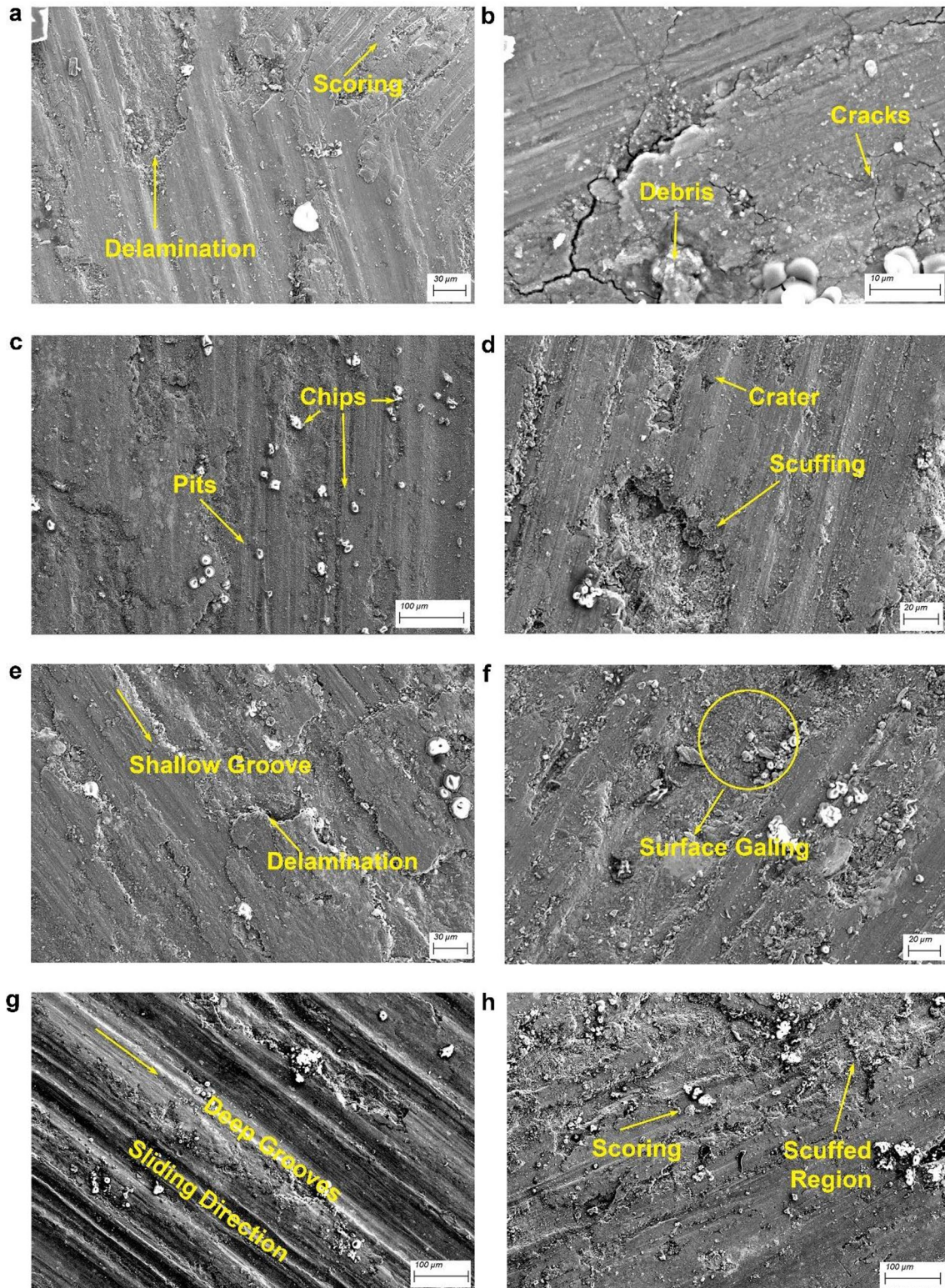
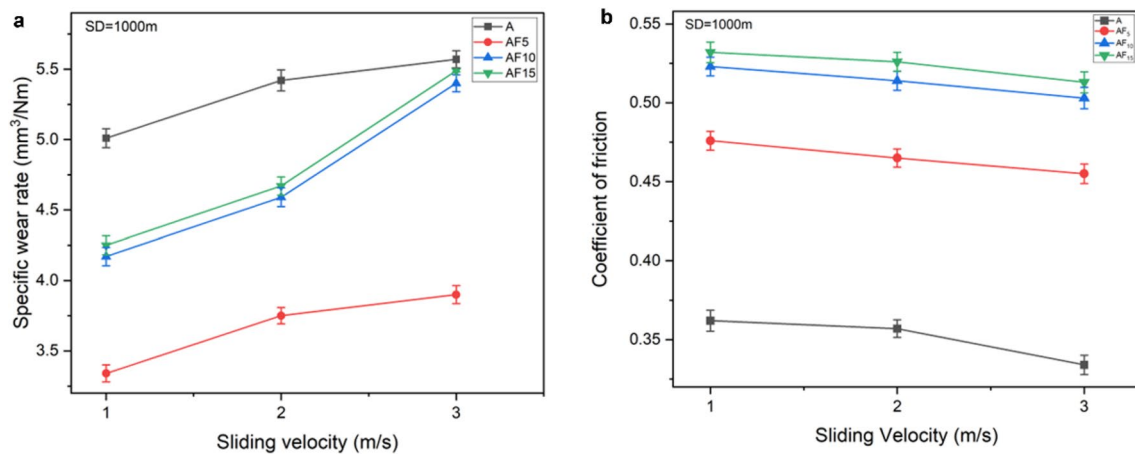


Fig. 10 FESEM analysis of worn-out surface for **a** sample A at 5 N **b** sample A at 15 N **c** sample AF₅ at 5N **d** sample AF₅ at 15N **e** sample AF₁₀ at 5N **f** sample AF₁₀ at 15N **g** sample AF₁₅ at 5N **h** sample AF₁₅ at 15N

Table 5 Average specific wear rate and coefficient of friction for varying sliding velocity

Sample No	Sample code	Load (N)	Sliding velocity (m/s)	Average specific wear rate $\times 10^{-5}$ (mm ³ /Nm)	Coefficient of friction (COF)
4	A	15	1	5.00 ± 0.13	0.362 ± 0.0023
5	A	15	2	5.43 ± 0.31	0.357 ± 0.0126
6	A	15	3	5.61 ± 0.55	0.354 ± 0.0512
10	AF5	15	1	3.34 ± 0.13	0.476 ± 0.0021
11	AF5	15	2	3.75 ± 0.39	0.465 ± 0.0061
12	AF5	15	3	3.91 ± 0.14	0.455 ± 0.0081
16	AF10	15	1	4.17 ± 0.19	0.523 ± 0.0071
17	AF10	15	2	4.59 ± 0.15	0.514 ± 0.0113
18	AF10	15	3	5.43 ± 0.121	0.503 ± 0.0103
22	AF15	15	1	4.31 ± 0.16	0.532 ± 0.0183
23	AF15	15	2	4.72 ± 0.11	0.526 ± 0.0119
24	AF15	15	3	5.56 ± 0.121	0.513 ± 0.0623

**Fig. 11** Impact of sliding velocity on the base material and developed composite specimens **a** Specific wear rate; **b** Coefficient of friction

3.3.3 Influence of Sliding Velocity on the Wear Rate and Friction Coefficient

Table 5 shows the average SWR and coefficient of friction values for the developed alloy and MMCs for varying sliding velocity and a static sliding distance of 1000 m and an applied load of 15N. It is noted that, as sliding velocity increases, the average SWR and COF considerably change.

Figure 11a illustrates the specific wear rate of the developed composite specimens and base material worn at a normal load of 15 N and under various sliding velocities (1 m/s, 2 m/s, and 3 m/s). Among the evaluated specimens, the base material exhibited a maximum wear rate of 0.00005 mm³/Nm at a sliding velocity of 1 m/s. At a sliding velocity of 1 m/s, a linear relationship was observed between the proportion of reinforcements and the wear rate of the specimens. The specimen AF₅ had the lowest wear rate, 33.2% less than the base material at 0.00005 mm³/Nm. A similar pattern was seen at a sliding velocity of 2 m/s.

The specimen AF₅ had the lowest wear rate of 0.0000375 mm³/Nm, while the base material had the highest wear rate of 0.0000543 mm³/Nm. Under the sliding velocity of 2 m/s, there was only a small difference in the wear rate between the specimens AF₅ and AF₁₀ (18.3%). The base material and the developed composite specimens exhibited a sharp increase in specific wear rate at the sliding velocity of 3 m/s. Compared to the base material-specific wear rate at 1 m/s, the base material wear rate at 3 m/s was 0.0000561 mm³/Nm (~ 12.2% higher). Similarly, the wear rates of the specimens AF₅, AF₁₀, and AF₁₅ worn at 3 m/s were higher than those of AF₅, AF₁₀, and AF₁₅ worn at 1 m/s.

Figure 11b shows the coefficients of friction of the base material and developed composite specimens under various sliding velocities (1 m/s, 2 m/s, and 3 m/s) and at a normal load of 15 N. At all the tested sliding velocities; the base material exhibited the least coefficient of friction (0.325 and 0.375). The specimen AF₅ had a lower coefficient of friction (0.45–0.475) than the specimens AF₁₀ and AF₁₅ at all the

sliding velocities. For any of the sliding velocities, the coefficient of friction did not significantly differ for the specimens AF₁₀ and AF₁₅. For the specimens AF₁₀ and AF₁₅, the coefficient of friction ranged between 0.53 and 0.54. For all of the examples, the general trend was that the coefficient of friction decreased as the sliding velocity increased from 1 m/s and 3 m/s. The following section describes the contributing variables to the wear phenomena.

3.3.4 Wear Mechanism Associated with Sliding Velocity Variation

Figure 11a, b demonstrates, respectively, the worn surface morphology of the base material at a sliding velocity of 1 m/s and 3 m/s. Cracks and debris were observed on the worn surface of the base material at a sliding velocity of 1 m/s. The worn surface showed high-order adhesive wear. Figure 12a shows that the concentration of O was lower than that of Al and Fe. The Al/Fe concentration ratio to O concentration did not sufficiently describe the generation of oxides. The Fe peaks corresponded to the partial diffusion of Fe towards the specimen from the counter disc. At the sliding velocity of 3 m/s, delamination, and grooves were seen on the base material's worn surface, as illustrated in Fig. 14b. The physical features show that the base material had experienced high-order adhesive wear. Consequently, the peaks broadened in the XRD graph, as shown in Fig. 13. Also, no steady peaks were observed to confirm the presence of Fe oxides.

At the sliding velocity of 1 m/s, scratches and scuffs were seen on the worn surface of the specimen AF₅, as illustrated in Fig. 14c. The specimen AF₅ has a lesser fraction of grazed zone than the base material. The specimen AF₅ had therefore been subjected to a mild adhesive wear regime. The damaged surface revealed high-order adhesive wear. Figure 12b demonstrates that O concentration was lower than Al and Fe. The production of oxides was not well elucidated by the ratio of Al/Fe concentration to O concentration. The Fe peaks indicated the partial diffusion of Fe from the counter disc towards the specimen.

Moreover, with the sliding velocity of 3 m/s, an extended spalled region and parallel score marks were seen on the surface in Fig. 14d. The characteristics of the specimen AF₅ show modest adhesive wear, and as a result, the peaks in the XRD graph widened, as depicted in Fig. 13. Nevertheless, no steady peaks indicated the existence of Fe oxides. Consistently, for sliding velocities of 1 m/s and 3 m/s, respectively, the wear rate of the specimen AF₅ was 32% and 30.35% less than the base material.

Figure 14e illustrates the worn surface morphology of the specimen AF₁₀ under the sliding velocity of 1 m/s, which exhibited shallow grooves. Narrow grooves and delamination are signs of a wear mechanism that transitions from mild adhesive wear to severe adhesive wear. As a result, with the sliding velocity of 1 m/s, the wear rate was 24.85% greater than the specimen AF₅. The lesser O concentration (relative to Al and Fe), as shown in Fig. 12c, indicated the absence of surface oxidation throughout the wear test.

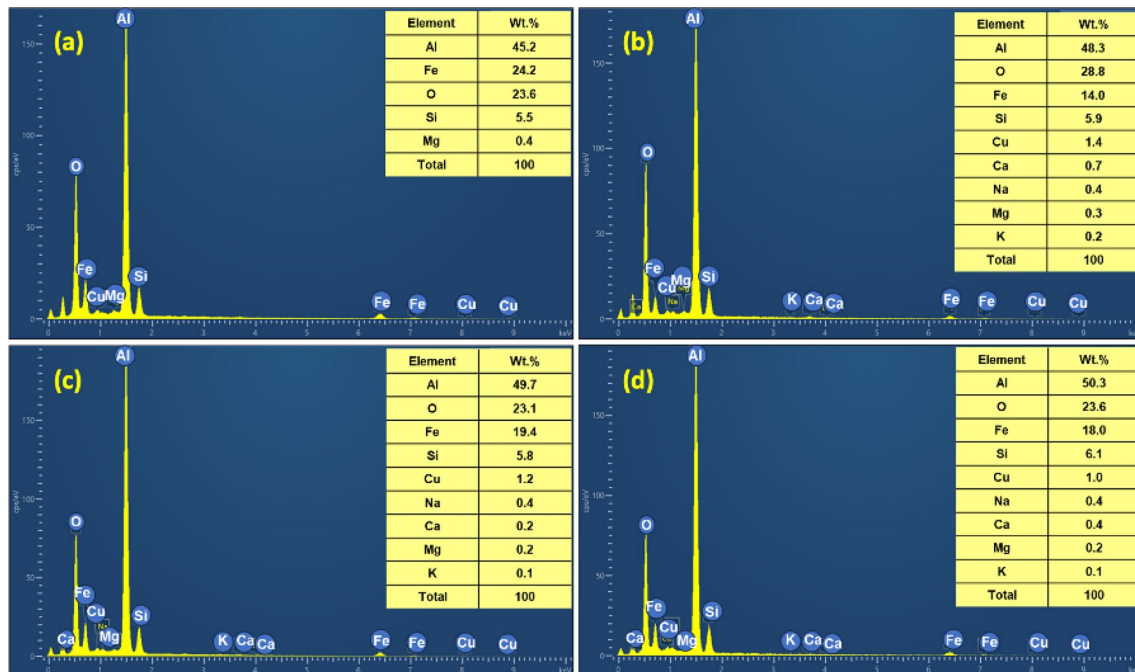
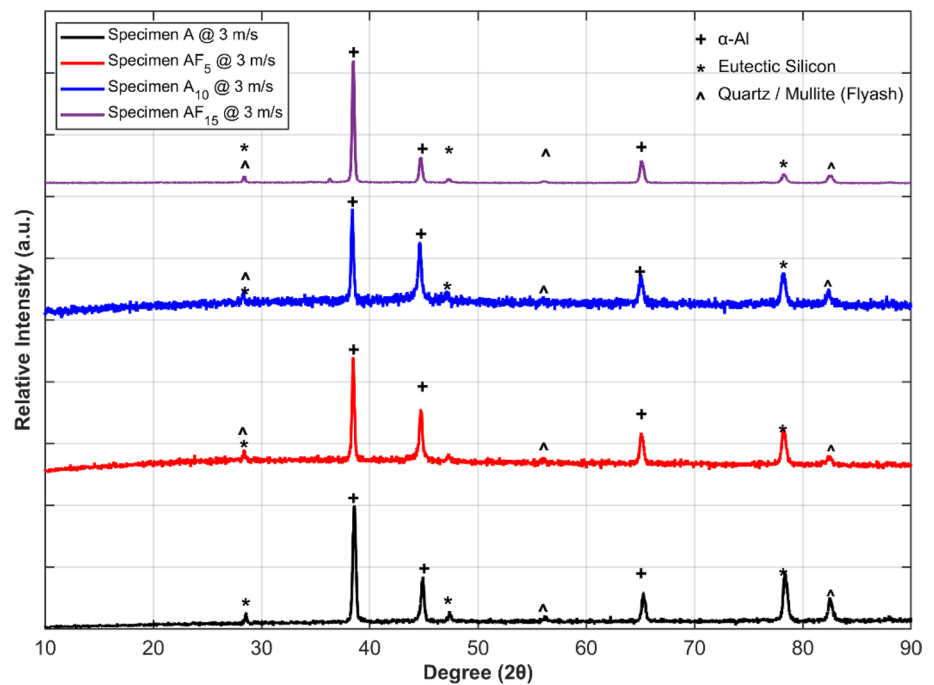


Fig. 12 Elemental composition at a sliding velocity of 1 m/s **a** Specimen A; **b** Specimen AF5; **c** Specimen AF10; **d** Specimen AF15

Fig. 13 XRD analysis of developed alloy and composites for high specific wear rate at 3 m/s



Also, Fe had partially diffused into the specimen AF₅. Going through abrasion on the specimen AF₁₀, depicted in Fig. 14f, demonstrated a transition from mild to severe adhesive wear at a sliding velocity of 3 m/s. The worn debris accelerated the elimination of material during the tribology test, which led to severe adhesive wear of the specimen. The peaks in the XRD graph, as shown in Fig. 13, broadened because of the severe adhesive wear of the specimen AF₁₀. Also, no significant peaks were observed to suggest the formation of Fe oxides. Al₂O₃ peaks were mostly accredited to the reinforcement particles (fly ash).

With the sliding velocity of 1 m/s, deep grooves were shown in Fig. 14g on the worn surface of the specimen AF₁₅. As the specimen AF₁₅ slid over the wear debris and up against the counter disc, reinforcing particles were removed in the form of wear debris, which is attributed to the development of grooves. O content was lower than Al and Fe, as observed in Fig. 12d. The ratio of Al/Fe concentration to O concentration could not explicate the generation of oxides. The Fe peaks revealed the partial diffusion of Fe from the counter disc towards the specimen. The distinctive characteristics to the phenomena of abrasive wear of the specimen AF₁₅ at a sliding of 3 m/s, (Fig. 14h). The high wear rate of the specimen is often linked to the abrasive wear mechanism. However, specimen AF₁₅ had a reduced wear rate compared to the base material (high-order adhesive wear). Due to the significant deformation of the specimen AF₁₅, the peaks in the XRD graph shown in Fig. 13 widened. Moreover, no notable peaks indicated the generation of Fe oxides. The Al₂O₃ peaks were attributed to the reinforcing particles (fly ash).

4 Conclusions

Aluminium alloy (A354) was successfully reinforced with varying percentages of fly ash (5%, 10%, 15%) through a liquid metallurgy process. The study focussed on assessing the resulting composite specimens' microstructure, microhardness, and dry sliding wear characteristics, including specific wear rate and coefficient of friction. The results demonstrated the following:

- Microstructure analysis confirmed the existence of α-Al, eutectic Si phase, and fly ash particles. The specimen AF₅ displayed uniform particle dispersion, while AF₁₅ exhibited particle agglomeration.
- Microhardness was enhanced in specimens AF5 and AF10 compared to the base material but decreased in AF₁₅ due to particle agglomeration.
- The lowest specific wear rate occurred at a high normal load of 15 N and a sliding velocity of 3 m/s, with AF₅ exhibiting the best performance among the specimens. Conversely, the coefficient of friction was highest at a high normal load of 15 N and 3 m/s sliding, with the base material showing the lowest friction coefficient overall.
- The specific wear rate was minimized at a high sliding velocity of 3 m/s for all samples at a normal load of 15 N, and specimen AF₅ displayed the lowest wear rate among all specimens. Lastly, at a low sliding velocity of 1 m/s and a normal load of 15 N, the coefficient of friction was highest for all specimens, while the base material exhibited the lowest friction coefficient across all sliding velocities.

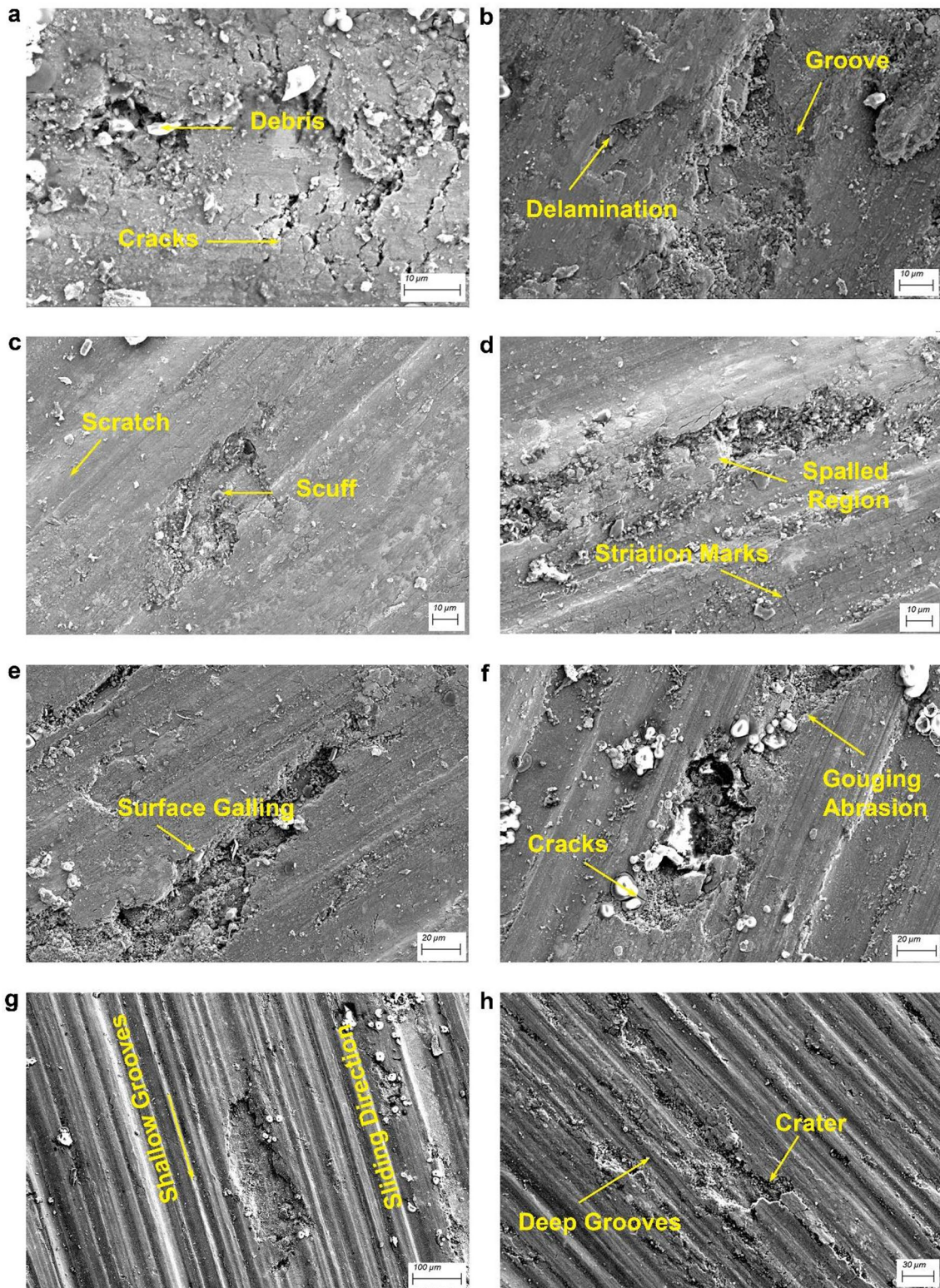


Fig. 14 FESEM analysis of worn-out surface for **a** sample A at 1 m/s **b** sample A at 3 m/s **c** sample AF₅ at 1 m/s **d** sample AF₅ at 3 m/s **e** sample AF₁₀ at 1 m/s **f** sample AF₁₀ at 3 m/s **g** sample AF₁₅ at 1 m/s **h** sample AF₁₅ at 3 m/s

Acknowledgements None.

Author Contributions All authors contributed to the study conception and design. Writing - original draft preparation was done by KVS. Writing - reviewing and editing was done by GKGP VV and JV. DP, MRL, AA, GR and RK prepared, collected data, and analysed. All authors read and approved the final manuscript.

Funding Not Applicable to this research.

Data Availability The data generated in this research are available upon request from the corresponding authors.

Declarations

Conflict of interest The authors declare that they have no known competing financial interests or personal relationships that could have appeared to influence the work reported in this paper.

Ethical Approval The present manuscript doesn't include any experiments with human members or animals conducted by any authors.

Consent to Participate All the authors give consent to participate in this study.

Consent for Publication All the authors give consent to publish in this journal if accepted.

References

- Shankar KV, Jezierski J, Ramalingam VV, Padmakumar D, Leena MR, Reghunath G, Krishnan R (2022) Investigating the effect of fly ash addition on the metallurgical and mechanical behavior of Al-Si-Mg-Cu alloy for engine cylinder head application. *Materials (Basel)* 15(15):5462. <https://doi.org/10.3390/ma15155462>
- Henriksson F, Johansen K (2016) On material substitution in automotive biws—from steel to aluminum body sides. *Procedia CIRP* 50:683–688. <https://doi.org/10.1016/j.procir.2016.05.028>
- Pana GM, Grigorie LD (2018) The issue of car body manufacture in unibody aluminum alloy. *Design Appl Mech Mater* 880:183–188. <https://doi.org/10.4028/www.scientific.net/AMM.880.183>
- Billy RG, Müller DB (2023) Aluminium use in passenger cars poses systemic challenges for recycling and GHG emissions. *Resour Conserv Recycl* 190:106827. <https://doi.org/10.1016/j.resconrec.2022.106827>
- Neto B, Kroeze C, Hordijk L, Costa C, Pulles T (2009) Strategies to reduce the environmental impact of an aluminium pressure die casting plant: a scenario analysis. *J Environ Manage* 90:815–830. <https://doi.org/10.1016/j.jenvman.2008.01.013>
- der Voet Van, Oers LV, Verboon M, Kuipers K (2018) Environmental implications of future demand scenarios for metals: methodology and application to the case of seven major metals. *J. Ind. Ecol.* 23:141–155. <https://doi.org/10.1111/jiec.12722>
- Modaresi R, Müller DB (2012) The role of automobiles for the future of aluminum recycling. *Environ Sci Technol* 46(16):8587–8594. <https://doi.org/10.1021/es300648w>
- Moors HM (2006) Technology strategies for sustainable metals production systems: a case study of primary aluminium production in The Netherlands and Norway. *J Clean Prod* 14:1121–1138. <https://doi.org/10.1016/j.jclepro.2004.08.005>
- Sathishkumar P, Deepakaravind V, Gopal P, Azhagiri P (2021) Analysis the mechanical properties and material characterization on magnesium metal matrix nano composites through stir casting process. *Mater Today Proc* 46:7436–7441. <https://doi.org/10.1016/j.matpr.2021.01.041>
- Nanjan S, Muralia JG (2020) Analysing the mechanical properties and corrosion phenomenon of reinforced metal matrix composite. *Materials Res* 23:e20190681. <https://doi.org/10.1590/1980-5373-mr-2019-0681>
- Mohana RD, Bandam BR (2014) Preparation and characterization of Al-fly ash metal matrix composite by stir casting method. *Int J Innov Sci Mod Eng* 3:1–5
- Zhou H, Bhattarai R, Li Y, Si B, Dong X, Wang T, Yao Z (2022) Towards sustainable coal industry: turning coal bottom ash into wealth. *Sci Total Environ* 804:149985. <https://doi.org/10.1016/j.scitotenv.2021.149985>
- Zhao H, Zhou F, Evelina LMA, Liu J, Zhou Y (2022) A review on the industrial solid waste application in pelletizing additives: composition, mechanism and process characteristics. *J Hazard Mater* 423:127056. <https://doi.org/10.1016/j.jhazmat.2021.127056>
- Ram AK, Mohanty S (2020) State of the art review on physicochemical and engineering characteristics of fly ash and its applications. *Int J Coal Sci Technol* 9:9. <https://doi.org/10.1007/s40789-022-00472-6>
- Luhar I, Luhar SA (2022) Comprehensive review on fly ash-based geopolymer. *J Compos Sci* 6:219. <https://doi.org/10.3390/jcs6080219>
- Yadav VK, Fulekar MH (2020) Advances in methods for recovery of ferrous, alumina, and silica nanoparticles from fly ash waste. *Ceramics* 3(3):384–420. <https://doi.org/10.3390/ceramics3030034>
- Ramamoorthi R, Hillary JJM, Sundaramoorthy R, Joseph JDJ, Kalidas K, Manickaraj K (2020) Influence of stir casting route process parameters in fabrication of aluminium matrix composites—A review. *Mater Today Proc* 45:6660–6664. <https://doi.org/10.1016/j.matpr.2020.12.068>
- Sharma DK, Badheka V, Patel V, Upadhyay G (2021) Recent developments in hybrid surface metal matrix composites produced by friction stir processing: a review. *J Tribol* 143:1–58. <https://doi.org/10.1115/1.4049590>
- Ravikumar KS, Ghanaraja S, Ramesh MR (2022) Effect of milling on the hardness and wear behaviour of cast Al6061 reinforced with Al₂O₃ nanoparticles. *J Bio Tribo Corros* 8:50801. <https://doi.org/10.1007/s40735-021-00598-1>
- Révész Á, Gajdics M (2021) Improved h-storage performance of novel mg-based nanocomposites prepared by high-energy ball milling: a review. *Energies* 14:6400. <https://doi.org/10.3390/en14196400>
- Aybarc U, Dispinar D, Seydibeyoglu MO (2018) Aluminum metal matrix composites with SiC, Al₂O₃ and graphene-review. *Arch Foundry Eng* 2:5–10
- Fan KL, He G, Liu X, Liu B, She M, Yuan Y, Yang Y, Lu Q (2013) Tensile and fatigue properties of gravity casting aluminum alloys for engine cylinder heads. *Mater Sci Eng A* 586:78–85. <https://doi.org/10.1016/j.msea.2013.08.016>
- Molina R, Amalberto P, Rosso M (2011) Mechanical characterization of aluminium alloys for high temperature applications part 1: Al-Si-Cu alloys. *Metall Sci Technol* 29:5–15
- Motta CAO, de Souza José, Martins V, Shaeffer L, Rossini EG, Biehl LV, Pacheco DAJ, Martins COD, Medeiros JLB (2023) Enhancing composite materials through fly ash reinforcement through powder metallurgy. *Mater Chem Phys* 3017:128124. <https://doi.org/10.1016/j.matchemphys.2023.128124>
- Venkatesh R, Sakthivel P, Selvakumar G, Krishnan AM, Purushothaman P, Priya CB (2023) Mechanical and thermal properties of a waste fly ash-bonded Al-10 Mg alloy composite improved by bioceramic silicon nanoparticles. *Biomass Conv Bioref.* <https://doi.org/10.1007/s13399-023-04588-w>

26. Debabrata P, Vijayakumar S, Rao TVJ, Babu RSR (2022) An examination of the tensile strength, hardness and SEM analysis of Al 5456 alloy by addition of different percentage of SiC/flyash. *Mater Today: Proc* 62:1995–1999. <https://doi.org/10.1016/j.matpr.2022.02.288>
27. Son HW, Lee JY, Cho Y-H, Jang J, Kim S-B, Lee J-M (2023) Enhanced mechanical properties and homogeneous T5 age-hardening behavior of Al-Si-Cu-Mg casting alloys. *J Alloys Compd* 960:170982. <https://doi.org/10.1016/j.jallcom.2023.170982>
28. Zang R, Ding L, Ehlers FJH, Jia Z, Xu S, Li Y, Cao L (2023) The influence of Cu content and Mg/Si ratio on the strength and formability in Al-Mg-Si-Cu alloys. *Mater Charact* 205:113355. <https://doi.org/10.1016/j.matchar.2023.113355>
29. De Oliveira LB, de Azevedo ARG, Marvila MT, Pereira EC, Fediuk R, Vieira CMF (2022) Durability of geopolymers with industrial waste. *Case Stud Constr Mater* 16:e00839. <https://doi.org/10.1016/j.cscm.2021.e00839>
30. Ganesh MRS, Reghunath NJ, Levin M, Prasad A, Doondi S, Shankar KV (2022) Strontium in Al–Si–Mg Alloy: a review. *Met Mater Int* 28:1–40. <https://doi.org/10.1007/s12540-021-01054-y>

Publisher's Note Springer Nature remains neutral with regard to jurisdictional claims in published maps and institutional affiliations.

Springer Nature or its licensor (e.g. a society or other partner) holds exclusive rights to this article under a publishing agreement with the author(s) or other rightsholder(s); author self-archiving of the accepted manuscript version of this article is solely governed by the terms of such publishing agreement and applicable law.